

## THERMAL AND NON-THERMAL EMISSION FROM A PECULIAR LONG-DURATION GRB 211211A

XUE-ZHAO CHANG<sup>1</sup>, HOU-JUN LÜ<sup>1</sup>, XING YANG<sup>1</sup>, JIA-MING CHEN<sup>2</sup>, AND EN-WEI LIANG<sup>1</sup>

## ABSTRACT

Long-duration GRB 211211A that lacks a supernova emission even down to very stringent limits at such a low redshift  $z = 0.076$  and associated with kilonova emission, suggest that its physical origin is from binary compact stars merger. By re-analyzing its data observed with the GBM on board Fermi mission, we find that both time-integrated and time-resolved spectra can be fitted well by using 2SBPL plus blackbody 2SBPL+BB model in the prompt emission. The bulk Lorentz factors ( $\Gamma_{\text{ph}}$ ) of the outflow can be inferred by invoking the observed thermal emission at photosphere radius within a pure fireball model, and find out that the temporal evolution of  $\Gamma_{\text{ph}}$  seems to be tracking with the light curve. The derived values of  $\Gamma_{\text{ph}}$  are also consistent with the  $\Gamma_{\text{ph}} - L_{\gamma, \text{iso}}/E_{\gamma, \text{iso}}$  correlations that had been found in other bursts. Moreover, we also calculate the magnetization factor  $\sigma_0$  in the central engine and  $\sigma_{\text{ph}}$  at the photosphere radius within the framework of hybrid jet model, and find that the values of both  $1 + \sigma_0$  and  $1 + \sigma_{\text{ph}}$  are larger than 1 for different time slices. It suggests that at least the Poynting-flux component is indeed existent in the outflow. If this is the case, one possible physical interpretation of thermal and non-thermal emissions in GRB 211211A is from the contributions of both  $\nu\bar{\nu}$  annihilation and the Blandford-Znajek mechanisms in the relativistic jet when a stellar mass black hole resides in the central engine.

*Subject headings:* Gamma-ray burst: general

## 1. INTRODUCTION

The field studying of gamma-ray bursts (GRBs) has made a great progress in both observations and theories (see Kumar & Zhang 2015, for a review). In general, GRBs are thought to be from a catastrophic event (such as massive star core collapse or merger of two compact stars) to release its gravitational energy that converted in the form of thermal energy, and a central engine (black hole or neutron star) is formed after the catastrophic event (Eichler et al. 1989; Usov 1992; Thompson 1994; Dai & Lu 1998a,b; Popham et al. 1999; Narayan et al. 2001; Zhang & Mészáros 2001; Lei et al. 2009; Metzger et al. 2011; Bucciantini et al. 2012; Lü & Zhang 2014; Berger 2014; Lü et al. 2015). The fireball model is the most popular one to interpret both  $\gamma$ -ray emission and broadband afterglow emission of GRB phenomenon (Mészáros & Rees 1997; Sari et al. 1998; Mészáros 2002; Zhang & Mészáros 2004; Zhang et al. 2016). The observed prompt emission can be explained by photosphere with a quasi-thermal spectrum (Paczynski 1986; Goodman 1986), or internal shocks with a non-thermal electromagnetic radiation (Rees & Meszaros 1994), or dissipation of the magnetic energy with a non-thermal spectrum at a large radius (Zhang & Yan 2011).

Within the above scenario, the photons that are produced in the thermalized outflow can escape near the photospheric radius when the optical depth is close to 1, and a purely quasi-thermal component should be observed in the prompt emission of GRB, such as GRB 090902B (Abdo et al. 2009; Ryde et al. 2010; Zhang et al. 2011). On the contrary, if the out-

flow is Poynting-flux dominated, it should produce a purely non-thermal emission, such as GRB 080916C (Zhang & Pe'er 2009). In general, the dissipated radius of photospheric and internal shock can not be distinguished very well, and the observed spectrum of GRB prompt emission should be the superposition of thermal and non-thermal components (Ryde 2005; Gao & Zhang 2015). Such evidence of thermal and non-thermal emission is already found in several solid cases, e.g., GRB 100724B (Guiriec et al. 2011); GRB 110721A (Axelsson et al. 2012); GRB 120323A (Guiriec et al. 2013); GBR 160625B (Lü et al. 2017); GRB 081221 (Hou et al. 2018).

Most recently, a peculiar and nearby long-duration GRB 211211A that triggered Fermi Gamma-Ray Burst Monitor (GBM; Mangan et al. 2021), Swift Burst Alert Telescope (BAT; D’Ai et al. 2021), as well as Insight-HXMT (Zhang et al. 2021), is very excited for attention with redshift  $z=0.076$ . The lightcurve of prompt emission is composed of an initial hard-main emission (with a duration  $\sim 13$  s) followed by a series of soft gamma-ray extended emission (EE) with a duration  $\sim 55$  s, and the structure of the lightcurve is similar to the particularly interesting case GRB 060614 (Yang et al. 2022; Xiao et al. 2022) and GRB 211227A (Lü et al. 2022). More interestingly, no associated supernova signature is detected for GRB 211211A, even down to very stringent limits at such a low redshift, but associated with kilonova is observed by several optical telescopes (Rastinejad et al. 2022). Those observed evidence suggest that GRB 211211A is originated from binary compact star merger (Rastinejad et al. 2022; Yang et al. 2022; Xiao et al. 2022; Gompertz et al. 2022). However, how to produce such long-duration emission within the compact stars merger scenario remains an open question. ? proposed that the black hole central engine surrounded by a strong magnetic flux can well interpret

<sup>1</sup> Guangxi Key Laboratory for Relativistic Astrophysics, School of Physical Science and Technology, Guangxi University, Nanning 530004, China; lhj@gxu.edu.cn

<sup>2</sup> School of Physics and Astronomy, Yunnan University, Kunming 650500, China

the behavior of long-duration emission of GRB 211211A. Gompertz et al. (2022) found that the spectrum can be fitted well with a double smoothly broken power-law model SBPL, which is interpreted as synchrotron emission, including both characteristic synchrotron frequency ( $\nu_m$ ) and the cooling frequency ( $\nu_c$ ). So that, identifying the composition of the jet in such a binary system will play an important role in understanding the physical process and mechanism (Zhang et al. 2011; Kumar & Zhang 2015; Zhang 2018).

In this paper, by analyzing the data observed with the GBM on board the Fermi mission, we find that a blackbody emission with a non-thermal component 2SBPL function can be fitted well to the spectra in the prompt emission of GRB 211211A, especially in the initial hard-main emission phase. It means that the thermal component should be indeed existence, and it is different from previous studies that claimed the single non-thermal component is dominated in the prompt emission phase (Yang et al. 2022; Xiao et al. 2022). The data analysis and spectral fitting are presented in §2. In §3, we derive the Lorentz factor of jet, its photospheric radius, magnetization  $\sigma_0$ , and the dimensionless entropy  $\eta$  based on the observed thermal and non-thermal emissions of GRB 211211A. The conclusions are drawn in §4 with some additional discussion. Throughout the paper, a concordance cosmology with parameters  $H_0 = 70 \text{ km s}^{-1} \text{ Mpc}^{-1}$ ,  $\Omega_M = 0.30$ , and  $\Omega_\Lambda = 0.70$  is adopted.

## 2. FERMI/GBM DATA ANALYSIS

### 2.1. Light curve and spectral fits

GRB 211211A triggered the Fermi/GBM at 13:09:59.651 UT on 11 December 2021 (Mangan et al. 2021). This GRB was also detected by Swift/BAT (D’Ai et al. 2021) and Insigt-HXMT (Zhang et al. 2021). We downloaded the corresponding Time-Tagged-Event data of GRB 211211A from the public science support center at the official Fermi Web site<sup>3</sup>. The GBM has 12 sodium iodide (NaI) detectors covering an energy range from 8 keV to 1 MeV, and two bismuth germanate (BGO) scintillation detectors sensitive to higher energies between 200 keV and 40 MeV (Meegan et al. 2009). We select the brightest NaI and BGO detectors for the analyses, namely n2, na and b0. For more details of data reduction of the light-curve, please refer to Lü et al. (2017) and Zhang et al. (2018).

We extract the light curves with a 128 ms time-bin (Figure 1) by running *gtbin*. The light curve shows a complex structure with a total duration of about  $T_{90} \sim 43$  s, an initially main emission (with a duration  $\sim 13$  s) followed by a series of soft gamma-ray extended emission with a duration  $\sim 55$  s (also see Yang et al. 2022).

Both time-integrated and time-resolved spectra of this source are extracted from the time-tagged event (TTE) data. The background spectrum from the GBM data is extracted from the continuous spectroscopy (CSPEC) format data with two time intervals before and after the prompt emission phase and are modeled with a polynomial function. We perform the spectral fit with the multi-mission maximum likelihood framework package

(3ML; Vianello et al. 2017), which adopts the Markov Chain Monte Carlo (MCMC) technique to perform time-resolved spectral fitting. Also, we evaluate the goodness of our fits with the maximum likelihood based statistics, the so-called PGSTAT. Yang et al. (2022) invoked a cut-off power-law model to do the spectral fitting in both time-averaged and time-resolved of GRB 211211A (also see Gompertz et al. 2022). In our analysis, several spectral models can be selected to test the spectral fitting of the burst, such as cutoff power-law (CPL), Band function (Band), a smoothly broken power law model (SBPL), a double smoothly broken power-law model (2SBPL) and Blackbody (BB), as well as combinations of any two models. The Band function (Band et al. 1993) and blackbody function, and CPL models are written as follows.

$$N_{\text{Band}}(E) = A \begin{cases} (\frac{E}{100 \text{ keV}})^\alpha \exp\left[-\frac{(\alpha+2)E}{E_p}\right], & E < E_c, \\ (\frac{E}{100 \text{ keV}})^\beta \exp(\beta - \alpha) (\frac{E_c}{100 \text{ keV}})^{\alpha-\beta}, & E \geq E_c \end{cases} \quad (1)$$

where  $A$  is the normalization of the spectrum,  $\alpha$  and  $\beta$  are the low and high energy photon spectral indices, respectively;  $E_p = (2 + \alpha)E_c$  is the peak energy.

$$N_{\text{BB}}(E) = A(t) \frac{E^2}{\exp[E/kT] - 1} \quad (2)$$

where  $k$  and  $T$  are Boltzmann constant and temperature, respectively.

$$N_{\text{CPL}}(E) = A \cdot E^{-\alpha} \exp(-\frac{E}{E_p}). \quad (3)$$

The SBPL function (Kaneko et al. 2006) function is defined as follows.

$$N_{\text{SBPL}}(E) = A \left( \frac{E}{100 \text{ keV}} \right)^b 10^{(a-a_{\text{piv}})} \quad (4)$$

where  $a = m\Lambda \ln\left(\frac{e^q + e^{-q}}{2}\right)$ ,  $a_{\text{piv}} = m\Lambda \ln\left(\frac{e^{q_{\text{piv}}} + e^{-q_{\text{piv}}}}{2}\right)$ ,  $q = \frac{\log(E/E_b)}{\Lambda}$ ,  $q_{\text{piv}} = \frac{\log(100 \text{ keV}/E_b)}{\Lambda}$ ,  $m = \frac{\beta - \alpha}{2}$ ,  $b = \frac{\alpha + \beta}{2}$ . Here,  $\alpha$ ,  $\beta$  and  $E_b$  are the lower power-law index, upper power-law index, and a break energy, respectively.  $\Lambda$  is the break scale which fixed at 0.3.

The 2SBPL function (Kaneko et al. 2006) function is defined as follows.

$$N_{2\text{SBPL}} = AE_b^{\alpha_1} [f_1(E) + f_2(E)]^{-\frac{1}{n_2}} \quad (5)$$

where  $f_1(E) = [(\frac{E}{E_b})^{-\alpha_1 n_1} + (\frac{E}{E_b})^{-\alpha_2 n_2}]^{n_2/n_1}$ ,  $f_2(E) = (\frac{E}{E_j})^{-\beta n_2} [(\frac{E_j}{E_b})^{-\alpha_1 n_1} + (\frac{E_j}{E_b})^{-\alpha_2 n_2}]^{n_2/n_1}$ , and  $E_j = E_{\text{pk}} \cdot \left(-\frac{\alpha_2 + 2}{\beta + 2}\right)^{\frac{1}{(\beta - \alpha_2)n_2}}$ .  $\alpha_1$  and  $\alpha_2$  are the photon index below and above the break energy, respectively.  $E_b$  and  $E_{\text{pk}}$  are the break energy and peak energy, respectively.  $\beta$  is the high-energy photon index above the peak energy.  $n_1$  (for the break) and  $n_2$  (for the peak) are the smoothness parameters. In this work, we fix the  $n_1 = 5.38$  and  $n_2 = 2.69$ , respectively (Ravasio et al. 2018).

In order to test which model is the best fit with the data, we compare the goodness of the fits by invoking the Bayesian information criteria (BIC)<sup>4</sup>. For the specific definition of the goodness of data fitting by the empirical model, please refer to Li (2019). We find that

<sup>3</sup> <https://heasarc.gsfc.nasa.gov/FTP/fermi/data/gbm/daily/>

<sup>4</sup> BIC is a criterion to evaluate the best model fit among a fi-

the 2SBPL+BB model is the best one to adequately describe the observed data, and it means that the thermal emission component in GRB 211211A is significant presence (see Table 1). The spectral fitting result of time-integrated is shown in Figure 2. Moreover, we find that the photon indices of the time-integrated spectral are  $\alpha_1 = -0.6$  and  $\alpha_2 = -1.62$ , respectively. These values are consistent with the results in Gompertz et al. (2022), and it suggest that the non-thermal component may be originated from the synchrotron emission in the fast regime.

We also extract time-resolved spectral analyses of GRB 211211A between  $T_0 + 0.5$  and  $T_0 + 70$ . We divide the time interval into 31 slices, and fit those slices by invoking 2SBPL and 2SBPL+BB models. The fitting results are shown in Table 2. Figure 1 shows the evolution of  $\Delta BIC$ , which is defined as  $\Delta BIC = BIC_{2SBPL} - BIC_{2SBPL+BB}$ . We find that the  $\Delta BIC$  of all time slices is larger than zero, especially, the  $\Delta BIC$  at the peak of light curve in both main emission and extended emission is much larger than 10. Even during the late period of the extended emission phase, the  $\Delta BIC$  of most time slices remains in the range of [6-10]. By comparing the BIC of 2SBPL and 2SBPL+BB models, we find that it is strong to support the 2SBPL+BB model, which is better than 2SBPL model to describe the observed data during the time-resolved spectral of GRB 211211A. In other words, the thermal emission component in GRB 211211A remains a significant presence in the time-resolved spectrum. By adopting  $z = 0.076$  of GRB 211211A, the total isotropic-equivalent energy ( $E_{\gamma,iso}$ ) and luminosity ( $L_{\gamma,iso}$ ) can be as high as  $7.6 \times 10^{51}$  erg and  $1.9 \times 10^{51}$  erg s $^{-1}$ , respectively.

### 2.2. Fitting results

In order to test the behavior of temporal evolution of main parameters for thermal and non-thermal emissions, we present the temporal evolution of  $E_b$ ,  $E_{pk}$ ,  $kT$ , the flux of BB emission ( $F_{BB}$ ), and the ratio of  $F_{BB}$  and total observed flux ( $F_{obs}$ ) in Figure 3. By comparing the  $E_b$  and  $E_{pk}$  evolution of both 2SBPL and 2SBPL+BB models, we find that the  $E_b$  and  $E_{pk}$  evolution of 2SBPL+BB model are similar to that of 2SBPL model, and the behavior of its evolution seems to be tracking with pulses of light curve. The temperature ( $kT$ ) and the flux ( $F_{BB}$ ) of BB emission also exhibit the tracking behavior with its pulses. The  $F_{BB}$  can reach to as high as  $8.161 \times 10^{-6}$  erg cm $^{-2}$  s $^{-1}$ . We also calculate the total observed flux, which includes both thermal and non-thermal emission and find that the fraction of thermal emission flux ( $F_{BB}/F_{obs}$ ) can reach as high as  $\sim 0.2$ . The significant thermal component in the prompt emission is also independent to support the BB emission which should indeed be presented.

nite set of models, and the lowest BIC of a model is preferred (Neath & Cavanaugh 2012). The definition of BIC can be written as:  $BIC = -2\ln L + k \cdot \ln(n)$ , where  $k$  is the number of model parameters,  $n$  is the number of data points, and  $L$  is the maximum value of the likelihood function of the estimated model. (1) if  $0 < \Delta BIC < 2$ , the evidence against the model with higher BIC is not worth more than a bare mention; (2) if  $2 < \Delta BIC < 6$ , the evidence against the model with higher BIC is positive; (3) if  $6 < \Delta BIC < 10$ , the evidence against the model with higher BIC is strong; (4) if  $10 < \Delta BIC$ , the evidence against the model with higher BIC is very strong.

### 3. DERIVATION OF THE PHYSICAL PARAMETERS WITHIN THE FIREBALL MODELS

The initial Lorentz factor of a GRB jet is a very important parameter for understanding GRB physics, and is also very difficult to measure for most GRBs (Zhang 2018). In general, there are three methods which have been proposed to estimate the Lorentz factor. The first one is to use the high-energy cutoff of the prompt gamma-ray spectrum, which is from the pair production when the absorption optical depth is close to one (Fenimore et al. 1993; Lithwick & Sari 2001; Zhang & Pe'er 2009). The second approach to estimating the Lorentz factor is using the early afterglow light curves with a smooth onset bump that shows the signal of fireball deceleration (Sari & Piran 1999; Kobayashi & Zhang 2007; Liang et al. 2010). The third one is using the blackbody component detected in some GRB spectra (Pe'er et al. 2007; Ryde et al. 2010; Gao & Zhang 2015). In this section, we derive the physical parameters based on the observed thermal component in prompt emission of GRB 211211A, such as the Lorentz factor ( $\Gamma_{ph}$ ) and the radius of photosphere ( $R_{ph}$ ). We also calculate the magnetization factor ( $\sigma_0$ ) and dimensionless entropy ( $\eta$ ) by assuming the hybrid jet of GRB 211211A.

#### 3.1. Lorentz Factor and Photosphere Radius

In our analyses, the time-resolved spectra of the GRB 211211A prompt emission is compose of a thermal component (BB component) and a non-thermal component (2SBPL component). Following the method of Pe'er et al. (2007), we estimate the  $\Gamma_{ph}$  and  $R_{ph}$  with the BB component derived from our spectral fits in different time slices,

$$\Gamma_{ph} = \left[ (1.06)(1+z)^2 D_L \frac{Y \sigma_T F_{obs}}{2 m_p c^3 \Re} \right]^{1/4} \quad (6)$$

where  $D_L$  is the luminosity distance,  $m_p$  is the proton mass,  $\sigma_T$  is the Thomson scattering cross-section, and  $F_{obs}$  is the observed total flux. In our calculation, we fix the  $Y = 1$  which is the ratio between the total fireball energy and the energy emitted in  $\gamma$ -ray. The definition of  $\Re$  is written as

$$\Re = \left( \frac{F_{BB}}{\sigma T^4} \right)^{1/2} \quad (7)$$

where  $\sigma$  and  $F_{BB}$  are the Stefan's constant and the observed blackbody component flux, respectively. On the other hand, the  $R_{ph}$  can be expressed as

$$R_{ph} = (L \sigma_T / 8 \pi \Gamma_{ph}^3 m_p c^3) \quad (8)$$

where  $L = 4 \pi D_L^2 F_{obs}$  is the luminosity that measured for bursts with known redshift. The calculation results are shown in Table 3.

Figure 4 shows the temporal evolution of  $\Gamma_{ph}$  and  $R_{ph}$ . During main emission phase, the evolution of  $\Gamma_{ph}$  is initially tracking with light curve, and maximum value can be reached as high as **311** at the peak of light curve. In the extended emission phase, the  $\Gamma_{ph}$  seems to be also tracking with the light curve, and it peaked at  $\Gamma_{ph} = 197$ , then, it is gradually going down to 91 until reaching the end of extended emission. As for the  $R_{ph}$ , the highest



value of  $R_{\text{ph}}$  is around  $\sim 2.55 \times 10^{10}$  cm and it keeps fluctuating around  $\sim 10^{10}$  cm.

### 3.2. Magnetization parameter and dimensionless entropy

One is different from the method of Pe'er et al. (2007) who inferred the central engine parameters by using the observed data within the framework of a pure fireball shock model. Gao & Zhang (2015) proposed a hybrid relativistic outflow of GRB (e.g., hot fireball component and Poynting-flux component), and developed a theory of its photosphere emission. One interesting question is that the observed non-thermal component of GRB 211211A is from the internal shock of fireball or another cold Poynting-flux component. Here, we infer the magnetization factor ( $\sigma_0$ ) and dimensionless entropy ( $\eta$ ) by assuming the hybrid jet of GRB 211211A.

The magnetization factor  $\sigma_0$  is defined as  $\sigma_0 = L_c/L_h$ , where the  $L_h$  and  $L_c$  are the luminosity of hot fireball component and cold poynting-flux component, respectively. The dimensionless entropy  $\eta$  can be defined as  $\eta = L_h/\dot{M}c^2$ , where  $\dot{M}$  is accretion rate. The time-varying of ( $\eta$ ,  $\sigma_0$ ) pair at the central engine can result in the evolution of the photosphere emission proprieties. Based on the results of derivation in Gao & Zhang (2015), several situations of different ( $\eta$ ,  $\sigma_0$ ) pairs are considered. (1)  $\eta \gg 1, \sigma_0 \ll 1$ : it means that the photosphere emission is dominated by a pure fireball component. (2)  $\eta \sim 1, 1 + \sigma_0 \gg 1$ : a Poynting-flux-dominated outflow, no detect any thermal component in GRB spectrum. By invoking the 'top-down' approach and based on the judgment criteria proposed by Gao & Zhang (2015), we can infer the parameters of the central engine by using the observed quasi-thermal photosphere emission parameters (such as  $F_{\text{BB}}$ ,  $F_{\text{obs}}$ , and  $kT$ ). However, the inferred parameters of the central engine are sensitive dependent on the selected initial radius ( $r_0$ ) of the central engine. For convenience, we adopt the initial radius  $r_0 = 10^7$  cm, and one can obtain all the photosphere characteristic parameters of the hybrid model (e.g.,  $\eta$ ,  $1 + \sigma_0$ ,  $R_{\text{ph}}$ ,  $\Gamma_{\text{ph}}$ , and  $1 + \sigma_{\text{ph}}$ ). Here,  $1 + \sigma_{\text{ph}}$  is the magnetization parameter at  $R_{\text{ph}}$ .

Figure 4 also shows the comparisons of  $\Gamma_{\text{ph}}$  and  $R_{\text{ph}}$  evolution for both pure fireball model and hybrid jet model with fixed  $r_0 = 10^7$  cm. It is interesting that the  $\Gamma_{\text{ph}}$  evolution behavior of a pure fireball model is similar to that of the hybrid jet model, and the evolution of  $R_{\text{ph}}$  is matched very well between those two models. Figure 5 presents the temporal evolution of  $1 + \sigma_0$  and  $\eta$  in the central engine with  $r = r_0$ , as well as  $1 + \sigma_{\text{ph}}$  at  $R_{\text{ph}}$ . The values of  $1 + \sigma_0$  and  $\eta$  are larger than 1 and 10 for different time slices, respectively. It means that at least the Poynting-flux component is indeed existent in the central engine. Meanwhile, it is clear to see that the values of  $1 + \sigma_{\text{ph}}$  are larger than 1 for different time slices, and range in [1-50]. So that, those results suggest that the Poynting-flux component should always be a presence at the position of the central engine and photosphere radius. The observed thermal and non-thermal components in GRB 211211A seem to be from the contributions of hot fireball and Poynting-flux outflow, respectively.

### 3.3. $\Gamma_{\text{ph}} - E_{\gamma,\text{iso}}/L_{\gamma,\text{iso}}$ correlations

Liang et al. (2010) discovered a tight correlation between initial Lorentz factor  $\Gamma_0$  and isotropic  $\gamma$ -ray energy  $E_{\gamma,\text{iso}}$ , namely  $\Gamma_0 \propto E_{\gamma,\text{iso}}^{0.25}$ . Lü et al. (2012) also found another tight correlation of  $\Gamma_0$  and isotropic  $\gamma$ -ray luminosity  $L_{\gamma,\text{iso}}$ , e.g.,  $\Gamma_0 \propto L_{\gamma,\text{iso}}^{0.3}$ . Those two correlations can be interpreted well by using a neutrino-cooled hyper-accretion disk around a stellar mass black hole as the GRB central engine (Lü et al. 2012).

In order to test whether the  $\Gamma_{\text{ph}}$  from time-resolved BB emission and  $E_{\gamma,\text{iso}}/L_{\gamma,\text{iso}}$  of GRB 211211A are tracking similar correlations to above, Figure 6 shows the relationship between  $\Gamma_{\text{ph}}$  and  $E_{\gamma,\text{iso}}/L_{\gamma,\text{iso}}$ . Caution, we do not adopt the data from Liang et al. (2010) and Lü et al. (2012) to do the joint fitting, because they adopt different methods to estimate the Lorentz factor. However, we collect the data of time-resolved spectra in GRB 160625B, which has the thermal emission and use the same method (e.g., BB emission) to infer the Lorentz factor. So, we used  $\Gamma_{\text{ph}}$  in our fitting to replace  $\Gamma_0$  in Liang et al. (2010), and the data of GRB 160625B are taken from Wang et al. (2017). For the diagram of  $\Gamma_{\text{ph}} - L_{\gamma,\text{iso}}$ , we make a joint fitting of the two groups (GRB 160625B and GRB 211211A) with a power-law model and find  $\Gamma_{\text{ph}} \propto L_{\gamma,\text{iso}}^{0.24 \pm 0.01}$  with a Pearsons correlation coefficient of 0.96 and  $p < 10^{-4}$ . Also, applying the power-law fitting to  $\Gamma_{\text{ph}} - E_{\gamma,\text{iso}}$ , we find  $\Gamma_{\text{ph}} \propto E_{\gamma,\text{iso}}^{0.26 \pm 0.02}$  with a Pearsons correlation coefficient of 0.91 and  $p < 10^{-4}$ . Those two results are similar to that of Lü et al. (2012) and Liang et al. (2010), respectively. It suggests that the central of GRB 211211A may be a stellar mass black hole with a neutrino-cooled hyper-accretion disk.

## 4. CONCLUSION AND DISCUSSION

GRB 211211A was observed by Fermi/GBM, Swift/BAT, and Insign-HXMT to have a duration of  $\sim 84$  seconds at redshift  $z = 0.076$ , but the light curve is characterized by an initial hard-main emission (with a duration  $\sim 13$  s) followed by a series of soft gamma-ray extended emission with a duration  $\sim 55$  s. The structure of lightcurve is similar to the cases of GRB 060614 and GRB 211227A which are believed to be from the compact star merger (Yang et al. 2022; Xiao et al. 2022; Lü et al. 2022). The total isotropic-equivalent energy ( $E_{\gamma,\text{iso}}$ ) and luminosity ( $L_{\gamma,\text{iso}}$ ) are as high as  $7.6 \times 10^{51}$  erg and  $1.9 \times 10^{51}$  erg s $^{-1}$ , respectively. At such low redshift, it is surprising that deep searches of an underlying SN give null results, but associated with kilonova is observed by several optical telescopes (Rastinejad et al. 2022). Those observed evidence suggests that GRB 211211A is originated from binary compact star merger (Rastinejad et al. 2022; Yang et al. 2022; Xiao et al. 2022; Gompertz et al. 2022).

By re-analyzing the data observed with the GBM on board the Fermi mission, we find the following interesting results:

- We find that the 2SBPL+BB model is the best one to adequately describe the observed data in both time-integrated and time-resolved spectra in the prompt emission of GRB 211211A based on the BIC criterion, and it means that both thermal and

non-thermal components in GRB 211211A should be significant presence.

- The behavior of temporal evolution of  $E_b$ ,  $E_{pk}$  for 2SBPL function and  $kT$  for BB emission seem to be tracking with pulses of the light curve.
- By inferring the Lorentz factor  $\Gamma_{ph}$  and photosphere radius  $R_{ph}$  based on the observed BB emission within the framework of a pure fireball model, we find that the temporal evolution of  $\Gamma_{ph}$  seems to be tracking with the light curve, and its range from 87 to 311. However, the highest value of  $R_{ph}$  is around  $\sim 2.5 \times 10^{10}$  cm and it keeps fluctuating around  $\sim 10^{10}$  cm.
- By calculating the magnetization factor  $\sigma_0$  in the central engine and  $\sigma_{ph}$  at the photosphere radius within the framework of the hybrid jet model, we find that the values of both  $1 + \sigma_0$  and  $1 + \sigma_{ph}$  are larger than 1 for different time slices for fixed initial  $r_0 = 10^7$  cm, and its range of [1,120]. It means that at least the Poynting-flux component is indeed existent in both central engine and photosphere radius.
- Moreover, we also plot the diagrams of  $\Gamma_{ph} - E_{\gamma,iso}/L_{\gamma,iso}$ , and find the relationships as  $\Gamma_{ph} \propto E_{\gamma,iso}^{0.26 \pm 0.02}$  and  $\Gamma_{ph} \propto L_{\gamma,iso}^{0.24 \pm 0.01}$  for the time-resolved spectral data of GRB 211211A. Those two correlations are consistent with that of in Liang et al. (2010) and Lü et al. (2012), respectively. It suggests that the central of GRB 211211A may be a stellar mass black hole with a neutrino-cooled hyper-accretion disk.

If the central engine of GRB 211211A is a stellar mass black hole which is formed from binary compact star merger (?). Lei et al. (2017) proposed that two jet launching mechanisms, i.e.,  $\nu\bar{\nu}$  annihilation and the Blandford-Znajek (BZ; Blandford & Znajek 1977) process, are indeed considered to power thermal and non-thermal components in the relativistic jet, respectively.  $\nu\bar{\nu}$  annihilation mechanism liberates the gravitational energy from the accretion disk, and BZ mechanism extracts the spin energy from the Kerr black hole (Popham et al.

1999; Lee et al. 2000; Li & Paczyński 2000; Gu et al. 2006; Lei et al. 2009, 2013). In this scenario, the observed thermal and non-thermal emissions in GRB 211211A can be interpreted as follows. The jet of GRB 211211A can be launched from a hyper-accreting black hole via  $\nu\bar{\nu}$  annihilation and BZ mechanism. Initially, due to a very high accretion rate of the black hole, the  $\nu\bar{\nu}$  annihilation should be dominated. It can produce thermal emission when the photons escape the system at the photosphere radius, and the internal shock or Poynting-flux outflow is used to produce the non-thermal component. After tens of seconds, the  $\nu\bar{\nu}$  annihilation is not strong enough along with the decreasing of accretion rate. But the magnetic field of the black hole becomes gradually stronger due to storage time, and the BZ mechanism will be dominated. If this is the case, it is natural to explain the observed gradually-decreased thermal emission and gradually-increased non-thermal emission of GRB 211211A.

Alternatively, what we discussed above about the evidence of Poynting-flux existence (e.g., magnetization factor  $\sigma_0$ ) in our results is dependent on the selected  $R_0$  in the calculations of the hybrid model, and we fixed  $R_0 = 10^7$  cm in our calculations. For different selected  $R_0$ , such as  $R_0 = 10^8$  cm or  $R_0 = 10^9$  cm, it correspond to different values of  $\sigma_0$ . So, it is difficult to judge whether it is accompanied by Poynting-flux component in the jet. If this is the case, only  $\nu\bar{\nu}$  annihilation mechanism can interpret the observed thermal emission (from photosphere) and non-thermal emission (from internal shock).

To find out such a uniform model to explain all observed characteristics of GRB 211211A, of course, is not an easy task. We therefore encourage intense multi-band follow-up observations for GRB 211211A-like events in the future.

We are very grateful to thank the referee for helpful comments and suggestions to improve this manuscript. We acknowledge the use of the public data from the Fermi/GBM data archive. This work is supported by the National Natural Science Foundation of China (grant Nos. 11922301, and 12133003), the Program of Bagui Young Scholars Program (LHJ), and the Guangxi Science Foundation (grant No. 2017GXNSFFA198008).

## REFERENCES

- Abdo, A. A., Ackermann, M., Ajello, M., et al. 2009, *ApJ*, 706, L138. doi:10.1088/0004-637X/706/1/L138
- Axelsson, M., Baldini, L., Barbiellini, G., et al. 2012, *ApJ*, 757, L31. doi:10.1088/2041-8205/757/2/L31
- Band, D., Matteson, J., Ford, L., et al. 1993, *ApJ*, 413, 281. doi:10.1086/172995
- Berger, E. 2014, *ARA&A*, 52, 43.
- Blandford, R. D. & Znajek, R. L. 1977, *MNRAS*, 179, 433. doi:10.1093/mnras/179.3.433
- Bucciantini, N., Metzger, B. D., Thompson, T. A., et al. 2012, *MNRAS*, 419, 1537. doi:10.1111/j.1365-2966.2011.19810.x
- D’Ai, A., Ambrosi, E., D’Elia, V., et al. 2021, GRB Coordinates Network, Circular Service, No. 31202, 31202
- Dai, Z. G. & Lu, T. 1998a, *MNRAS*, 298, 87. doi:10.1046/j.1365-8711.1998.01681.x
- Dai, Z. G. & Lu, T. 1998b, *A&A*, 333, L87
- Eichler, D., Livio, M., Piran, T., et al. 1989, *Nature*, 340, 126. doi:10.1038/340126a0
- Fenimore, E. E., Epstein, R. I., & Ho, C. 1993, *A&AS*, 97, 59
- Gao, H. & Zhang B et al. 2015, *ApJ*, 801, 5. doi:10.1088/0004-637X/801/2/103
- Gao, H., Lei, W.-H., & Zhu, Z.-P. 2022, *ApJ*, 934, L12. doi:10.3847/2041-8213/ac80c7
- Gompertz, B. P., Rasio, M. E., Nicholl, M., et al. 2022, arXiv:2205.05008
- Goodman, J. 1986, *ApJ*, 308, L47. doi:10.1086/184741
- Guiriec, S., Connaughton, V., Briggs, M. S., et al. 2011, *ApJ*, 727, L33. doi:10.1088/2041-8205/727/2/L33
- Guiriec, S., Daigne, F., Hascoët, R., et al. 2013, *ApJ*, 770, 32. doi:10.1088/0004-637X/770/1/32
- Gu, W.-M., Liu, T., & Lu, J.-F. 2006, *ApJ*, 643, L87. doi:10.1086/505140
- Hou, S.-J., Zhang, B.-B., Meng, Y.-Z., et al. 2018, *ApJ*, 866, 13. doi:10.3847/1538-4357/aadc07
- Kumar, P. & Zhang, B. 2015, *Phys. Rep.*, 561, 1. doi:10.1016/j.physrep.2014.09.008
- Kobayashi, S. & Zhang, B. 2007, *ApJ*, 655, 973. doi:10.1086/510203

TABLE 1  
TIME-INTEGRAL SPECTRAL ANALYSIS RESULTS OF GRB 211211A.

$t_1 - t_2$ (s)	Model	$\alpha(\alpha_1)$	$E_b$ (keV)	$E_p/E_c$ (keV)	$\beta$	$\alpha_2$	kT (keV)	BIC	favourite model
0.5-70	Band	$-1.22^{+0.01}_{-0.01}$	...	$497^{+15}_{-15}$	$-2.21^{+0.03}_{-0.03}$	...	...	8633	
	CPL	$-1.27^{+0.01}_{-0.01}$	...	$916^{+19}_{-19}$	...	...	...	8964	
	BB	...	...	...	...	...	53	125651	
	Band+BB	$-1^{+0.01}_{-0.01}$	...	$175^{+6}_{-6}$	$-2.06^{+0.02}_{-0.02}$	...	$201^{+7}_{-7}$	7864	
	CPL+BB	$-1.08^{+0.01}_{-0.01}$	...	$250^{+5}_{-5}$	...	...	$312^{+5}_{-5}$	8149	
	SBPL	$-1.19^{+0.01}_{-0.01}$	$210^{+10}_{-11}$	...	$-2.11^{+0.02}_{-0.02}$	...	...	8523	
	SBPL+BB	$-0.96^{+0.02}_{-0.02}$	$81^{+4}_{-4}$	...	$-2.08^{+0.02}_{-0.02}$	...	$199^{+6}_{-6}$	7732	
	2SBPL	$-0.6^{+0.04}_{-0.04}$	$26.2^{+1.3}_{-1.3}$	$1020^{+40}_{-50}$	$-2.93^{+0.07}_{-0.07}$	$-1.59^{+0.01}_{-0.01}$	...	7461	
	2SBPL+BB	$-0.6^{+0.04}_{-0.04}$	$27^{+1.9}_{-1.8}$	$1200^{+110}_{-110}$	$-3.14^{+0.14}_{-0.13}$	$-1.62^{+0.02}_{-0.02}$	$77^{+16}_{-15}$	7443	✓

- Lee, H. K., Wijers, R. A. M. J., & Brown, G. E. 2000, Phys. Rep., 325, 83. doi:10.1016/S0370-1573(99)00084-8
- Lei, W. H., Wang, D. X., Zhang, L., et al. 2009, ApJ, 700, 1970. doi:10.1088/0004-637X/700/2/1970
- Lei, W.-H., Zhang, B., & Liang, E.-W. 2013, ApJ, 765, 125. doi:10.1088/0004-637X/765/2/125
- Lei, W.-H., Zhang, B., Wu, X.-F., et al. 2017, ApJ, 849, 47. doi:10.3847/1538-4357/aa9074
- Li, L.-X. & Paczyński, B. 2000, ApJ, 534, L197. doi:10.1086/312678
- Li, L. 2019, ApJS, 242, 16.
- Liang, E.-W., Yi, S.-X., Zhang, J., et al. 2010, ApJ, 725, 2209. doi:10.1088/0004-637X/725/2/2209
- Lithwick, Y. & Sari, R. 2001, ApJ, 555, 540. doi:10.1086/321455
- Lü, H.-J., Lü, J., Zhong, S.-Q., et al. 2017, ApJ, 849, 71. doi:10.3847/1538-4357/aa8f99
- Lü, H.-J. & Zhang, B. 2014, ApJ, 785, 74. doi:10.1088/0004-637X/785/1/74
- Lü, H.-J., Zhang, B., Lei, W.-H., et al. 2015, ApJ, 805, 89. doi:10.1088/0004-637X/805/2/89
- Lü, H.-J., Yuan, H.-Y., Yi, T.-F., et al. 2022, ApJ, 931, L23. doi:10.3847/2041-8213/ac6e3a
- Lü, J., Zou, Y.-C., Lei, W.-H., et al. 2012, ApJ, 751, 49. doi:10.1088/0004-637X/751/1/49
- Kaneko, Y., Preece, R. D., Briggs, M. S., et al. 2006, ApJS, 166, 298.
- Mangan, J., Dunwoody, R., Meegan, C., et al. 2021, GRB Coordinates Network, Circular Service, No. 31210, 31210
- Meegan, C., Lichti, G., Bhat, P. N., et al. 2009, ApJ, 702, 791. doi:10.1088/0004-637X/702/1/791
- Metzger, B. D., Giannios, D., Thompson, T. A., et al. 2011, MNRAS, 413, 2031. doi:10.1111/j.1365-2966.2011.18280.x
- Mészáros, P. & Rees, M. J. 1997, ApJ, 476, 232. doi:10.1086/303625
- Mészáros, P. 2002, ARA&A, 40, 137. doi:10.1146/annurev.astro.40.060401.093821
- Narayan, R., Piran, T., & Kumar, P. 2001, ApJ, 557, 949. doi:10.1086/322267
- Neath, A. A. & Cavanaugh, J. E. 2012, WIREs Comput. Stat., 4, 199. doi: 10.1002/wics.199
- Paczynski, B. 1986, ApJ, 308, L43. doi:10.1086/184740
- Pe'er, A., Ryde, F., Wijers, R. A. M. J., et al. 2007, ApJ, 664, L1. doi:10.1086/520534
- Popham, R., Woosley, S. E., & Fryer, C. 1999, ApJ, 518, 356. doi:10.1086/307259
- Ravasio, M. E., Oganessyan, G., Ghirlanda, G., et al. 2018, A&A, 613, A16.
- Rastinejad, J. C., Gompertz, B. P., Levan, A. J., et al. 2022, arXiv:2204.10864
- Rees, M. J. & Meszaros, P. 1994, ApJ, 430, L93. doi:10.1086/187446
- Ryde, F. 2005, ApJ, 625, L95. doi:10.1086/431239
- Ryde, F., Axelsson, M., Zhang, B. B., et al. 2010, ApJ, 709, L172. doi:10.1088/2041-8205/709/2/L172
- Sari, R., Piran, T., & Narayan, R. 1998, ApJ, 497, L17. doi:10.1086/311269
- Sari, R. & Piran, T. 1999, A&AS, 138, 537. doi:10.1051/aas:1999342
- Thompson, C. 1994, MNRAS, 270, 480. doi:10.1093/mnras/270.3.480
- Usov, V. V. 1992, Nature, 357, 472. doi:10.1038/357472a0
- Vianello, G., Lauer, R. J., Burgess, J. M., et al. 2017, Proceedings of the 7th International Fermi Symposium, 130
- Wang, Y.-Z., Wang, H., Zhang, S., et al. 2017, ApJ, 836, 81. doi:10.3847/1538-4357/aa56c6
- Xiao, S., Zhang, Y.-Q., Zhu, Z.-P., et al. 2022, arXiv:2205.02186
- Yang, Y., Zhang, B.-B., Shunke, Ai., et al. 2022, arXiv:2204.12771
- Zhang, B. 2018, The Physics of Gamma-Ray Bursts by Bing Zhang. ISBN: 978-1-139-22653-0. Cambridge Univeristy Press, 2018. doi:10.1017/9781139226530
- Zhang, B. & Pe'er, A. 2009, ApJ, 700, L65. doi:10.1088/0004-637X/700/2/L65
- Zhang, B. & Mészáros, P. 2001, ApJ, 552, L35. doi:10.1086/320255
- Zhang, B. & Mészáros, P. 2004, International Journal of Modern Physics A, 19, 2385. doi:10.1142/S0217751X0401746X
- Zhang, B. & Yan, H. 2011, ApJ, 726, 90. doi:10.1088/0004-637X/726/2/90
- Zhang, B., Lü, H.-J., & Liang, E.-W. 2016, Space Sci. Rev., 202, 3. doi:10.1007/s11214-016-0305-9
- Zhang, B.-B., Zhang, B., Liang, E.-W., et al. 2011, ApJ, 730, 141. doi:10.1088/0004-637X/730/2/141
- Zhang, B.-B., Zhang, B., Castro-Tirado, A. J., et al. 2018, Nature Astronomy, 2, 69. doi:10.1038/s41550-017-0309-8
- Zhang, Y. Q., Xiong, S. L., Li, X. B., et al. 2021, GRB Coordinates Network, Circular Service, No. 31236, 31236

TABLE 2  
THE FITTING RESULTS OF TIME-RESOLVED SPECTRAL WITH 2SBPL AND 2SBPL+BB IN GRB 211211A PROMPT EMISSION.

$t_1$		$t_2$		2SBPL			BIC (PGSTAT)	2SBPL + BB			BIC (PGSTAT)	$\Delta$ BIC			
s	s	$\alpha_1$	$\alpha_2$	$E_b$ (keV)	$E_{pk}$ (keV)	$\beta$		$\alpha_1$	$\alpha_2$	$E_b$ (keV)	$E_{pk}$ (keV)	$\beta$	kT(keV)		
0.5	1.5	-0.9 <sup>+0.5</sup> <sub>-0.5</sub>	-1.1 <sup>+0.6</sup> <sub>-0.5</sub>	13 <sup>+10</sup> <sub>-9</sub>	151 <sup>+24</sup> <sub>-60</sub>	-2.9 <sup>+0.5</sup> <sub>-0.5</sub>	1640.4(1605.2)	-0.9 <sup>+0.5</sup> <sub>-0.4</sub>	-1.1 <sup>+0.5</sup> <sub>-0.5</sub>	13 <sup>+9</sup> <sub>-9</sub>	121 <sup>+24</sup> <sub>-40</sub>	-3.1 <sup>+0.5</sup> <sub>-0.5</sub>	46 <sup>+19</sup> <sub>-19</sub>	1632.6(1585.7)	7.8
1.5	2.5	-0.9 <sup>+0.4</sup> <sub>-0.5</sub>	-1.07 <sup>+0.4</sup> <sub>-0.33</sub>	26 <sup>+15</sup> <sub>-13</sub>	820 <sup>+120</sup> <sub>-120</sub>	-2.52 <sup>+0.14</sup> <sub>-0.15</sub>	2001.2(1966.1)	-0.83 <sup>+0.34</sup> <sub>-0.5</sub>	-1.17 <sup>+0.5</sup> <sub>-0.3</sub>	27 <sup>+12</sup> <sub>-12</sub>	980 <sup>+210</sup> <sub>-210</sub>	-2.66 <sup>+0.22</sup> <sub>-0.22</sub>	65 <sup>+18</sup> <sub>-19</sub>	1999.9(1953.1)	1.3
2.5	3.5	-0.73 <sup>+0.9</sup> <sub>-0.01</sub>	-1.48 <sup>+0.1</sup> <sub>-0.1</sub>	98 <sup>+18</sup> <sub>-19</sub>	1370 <sup>+130</sup> <sub>-130</sub>	-3.2 <sup>+0.16</sup> <sub>-0.17</sub>	2594.7(2559.5)	-0.67 <sup>+0.04</sup> <sub>-0.04</sub>	-1.64 <sup>+0.04</sup> <sub>-0.04</sub>	92 <sup>+12</sup> <sub>-12</sub>	2100 <sup>+210</sup> <sub>-210</sub>	-3.99 <sup>+0.31</sup> <sub>-0.31</sub>	168 <sup>+17</sup> <sub>-16</sub>	2569.5(2522.6)	25.2
3.5	4.5	-0.6 <sup>+0.4</sup> <sub>-0.8</sub>	-1.09 <sup>+0.8</sup> <sub>-0.34</sub>	38 <sup>+5</sup> <sub>-5</sub>	840 <sup>+150</sup> <sub>-100</sub>	-2.88 <sup>+0.09</sup> <sub>-0.09</sub>	2327.8(2292.6)	-0.61 <sup>+0.33</sup> <sub>-0.8</sub>	-1.21 <sup>+0.8</sup> <sub>-0.35</sub>	42 <sup>+7</sup> <sub>-7</sub>	960 <sup>+190</sup> <sub>-190</sub>	-2.99 <sup>+0.18</sup> <sub>-0.14</sub>	100 <sup>+40</sup> <sub>-40</sub>	2326(2279.1)	1.8
4.5	5.5	-0.68 <sup>+0.13</sup> <sub>-0.12</sub>	-1.66 <sup>+0.06</sup> <sub>-0.08</sub>	38 <sup>+9</sup> <sub>-9</sub>	530 <sup>+80</sup> <sub>-80</sub>	-3.2 <sup>+0.4</sup> <sub>-0.4</sub>	2102.9(2067.7)	-0.69 <sup>+0.12</sup> <sub>-0.11</sub>	-1.71 <sup>+0.08</sup> <sub>-0.08</sub>	39 <sup>+9</sup> <sub>-9</sub>	570 <sup>+110</sup> <sub>-110</sub>	-3.3 <sup>+0.4</sup> <sub>-0.4</sub>	73 <sup>+26</sup> <sub>-30</sub>	2095.1(2048.2)	7.8
5.5	6.5	-0.62 <sup>+0.04</sup> <sub>-0.03</sub>	-1.55 <sup>+0.02</sup> <sub>-0.03</sub>	81 <sup>+9</sup> <sub>-9</sub>	1700 <sup>+100</sup> <sub>-100</sub>	-3.36 <sup>+0.14</sup> <sub>-0.14</sub>	2592.3(2557.2)	-0.59 <sup>+0.05</sup> <sub>-0.04</sub>	-1.55 <sup>+0.24</sup> <sub>-0.04</sub>	72 <sup>+9</sup> <sub>-9</sub>	1860 <sup>+170</sup> <sub>-160</sub>	-3.48 <sup>+0.17</sup> <sub>-0.18</sub>	126 <sup>+40</sup> <sub>-35</sub>	2579.9(2533.1)	12.4
6.5	7.5	-0.57 <sup>+0.12</sup> <sub>-0.03</sub>	-1.35 <sup>+0.05</sup> <sub>-0.1</sub>	70 <sup>+7</sup> <sub>-7</sub>	1630 <sup>+70</sup> <sub>-110</sub>	-3.09 <sup>+0.09</sup> <sub>-0.09</sub>	2751.6(2716.4)	-0.69 <sup>+0.25</sup> <sub>-0.7</sub>	-1.22 <sup>+0.7</sup> <sub>-0.24</sub>	67 <sup>+7</sup> <sub>-7</sub>	1750 <sup>+280</sup> <sub>-190</sub>	-3.12 <sup>+0.1</sup> <sub>-0.1</sub>	100 <sup>+60</sup> <sub>-50</sub>	2743.6(2696.7)	8
7.5	8.5	0.68 <sup>+0.29</sup> <sub>-0.8</sub>	-1.21 <sup>+0.8</sup> <sub>-0.28</sub>	57 <sup>+5</sup> <sub>-5</sub>	1440 <sup>+270</sup> <sub>-160</sub>	-3.34 <sup>+0.13</sup> <sub>-0.31</sub>	2539.6(2504.4)	-0.56 <sup>+0.2</sup> <sub>-0.05</sub>	-1.35 <sup>+0.09</sup> <sub>-0.2</sub>	55 <sup>+6</sup> <sub>-6</sub>	1670 <sup>+180</sup> <sub>-180</sub>	-3.64 <sup>+0.21</sup> <sub>-0.22</sub>	136 <sup>+24</sup> <sub>-23</sub>	2524.6(2477.7)	15
8.5	9.5	-0.5 <sup>+0.11</sup> <sub>-0.11</sub>	-1.67 <sup>+0.04</sup> <sub>-0.05</sub>	34 <sup>+5</sup> <sub>-5</sub>	660 <sup>+90</sup> <sub>-90</sub>	-3.2 <sup>+0.35</sup> <sub>-0.4</sub>	2090.2(2055.1)	-0.51 <sup>+0.11</sup> <sub>-0.11</sub>	-1.69 <sup>+0.05</sup> <sub>-0.06</sub>	35 <sup>+5</sup> <sub>-5</sub>	650 <sup>+120</sup> <sub>-100</sub>	-3.2 <sup>+0.4</sup> <sub>-0.4</sub>	80 <sup>+50</sup> <sub>-40</sub>	2080.5(2033.7)	9.7
9.5	10.5	-0.33 <sup>+0.11</sup> <sub>-0.11</sub>	-1.75 <sup>+0.04</sup> <sub>-0.04</sub>	33.4 <sup>+3.2</sup> <sub>-3.2</sub>	680 <sup>+120</sup> <sub>-130</sub>	-3.2 <sup>+0.4</sup> <sub>-0.4</sub>	2072.5(2037.3)	-0.34 <sup>+0.11</sup> <sub>-0.11</sub>	-1.76 <sup>+0.04</sup> <sub>-0.04</sub>	33.8 <sup>+3.4</sup> <sub>-3.4</sub>	690 <sup>+160</sup> <sub>-140</sub>	-3.2 <sup>+0.4</sup> <sub>-0.4</sub>	64 <sup>+31</sup> <sub>-33</sub>	2066.6(2019.8)	5.9
10.5	11.5	-0.41 <sup>+0.12</sup> <sub>-0.12</sub>	-1.8 <sup>+0.04</sup> <sub>-0.04</sub>	31 <sup>+3</sup> <sub>-3</sub>	590 <sup>+90</sup> <sub>-100</sub>	-3.9 <sup>+0.5</sup> <sub>-0.5</sub>	1991.1(1955.9)	-0.44 <sup>+0.12</sup> <sub>-0.12</sub>	-1.85 <sup>+0.07</sup> <sub>-0.08</sub>	32 <sup>+4</sup> <sub>-4</sub>	530 <sup>+150</sup> <sub>-170</sub>	-3.8 <sup>+0.5</sup> <sub>-0.5</sub>	90 <sup>+50</sup> <sub>-50</sub>	1981.1(1934.3)	10
11.5	12.5	-0.68 <sup>+0.21</sup> <sub>-0.19</sub>	-1.82 <sup>+0.07</sup> <sub>-0.14</sub>	26 <sup>+6</sup> <sub>-5</sub>	410 <sup>+170</sup> <sub>-220</sub>	-3 <sup>+0.7</sup> <sub>-0.7</sub>	1850.3(1815.1)	-0.68 <sup>+0.16</sup> <sub>-0.17</sub>	-1.89 <sup>+0.06</sup> <sub>-0.08</sub>	27 <sup>+5</sup> <sub>-5</sub>	450 <sup>+220</sup> <sub>-250</sub>	-3.1 <sup>+0.6</sup> <sub>-0.6</sub>	50 <sup>+23</sup> <sub>-22</sub>	1843.1(1796.2)	7.2
12.5	13.5	-0.56 <sup>+0.32</sup> <sub>-0.32</sub>	-1.83 <sup>+0.1</sup> <sub>-0.12</sub>	21 <sup>+5</sup> <sub>-5</sub>	540 <sup>+280</sup> <sub>-350</sub>	-2.9 <sup>+0.6</sup> <sub>-0.6</sub>	1711.8(1676.6)	-0.53 <sup>+0.3</sup> <sub>-0.29</sub>	-1.86 <sup>+0.09</sup> <sub>-0.11</sub>	20 <sup>+4</sup> <sub>-4</sub>	570 <sup>+300</sup> <sub>-400</sub>	-2.9 <sup>+0.6</sup> <sub>-0.6</sub>	45 <sup>+18</sup> <sub>-18</sub>	1703.9(1657.1)	7.9
13.5	15	-0.63 <sup>+0.23</sup> <sub>-0.25</sub>	-1.88 <sup>+0.07</sup> <sub>-0.08</sub>	22 <sup>+4</sup> <sub>-4</sub>	500 <sup>+270</sup> <sub>-310</sub>	-3 <sup>+0.6</sup> <sub>-0.6</sub>	2154.1(2118.8)	-0.65 <sup>+0.24</sup> <sub>-0.23</sub>	-1.86 <sup>+0.05</sup> <sub>-0.12</sub>	21 <sup>+4</sup> <sub>-4</sub>	530 <sup>+320</sup> <sub>-350</sub>	-3 <sup>+0.6</sup> <sub>-0.6</sub>	43 <sup>+18</sup> <sub>-18</sub>	2152.1(2105.3)	2
15	17	-0.53 <sup>+0.19</sup> <sub>-0.17</sub>	-1.81 <sup>+0.05</sup> <sub>-0.13</sub>	26 <sup>+4</sup> <sub>-4</sub>	600 <sup>+270</sup> <sub>-310</sub>	-2.8 <sup>+0.5</sup> <sub>-0.6</sub>	2624.1(2588.8)	-0.52 <sup>+0.15</sup> <sub>-0.16</sub>	-1.88 <sup>+0.06</sup> <sub>-0.07</sub>	26.1 <sup>+3.5</sup> <sub>-3.3</sub>	670 <sup>+310</sup> <sub>-350</sub>	-2.9 <sup>+0.6</sup> <sub>-0.6</sub>	46 <sup>+21</sup> <sub>-20</sub>	2618.4(2571.6)	5.7
17	19	-0.5 <sup>+0.1</sup> <sub>-0.1</sub>	-1.71 <sup>+0.04</sup> <sub>-0.04</sub>	32 <sup>+4</sup> <sub>-4</sub>	560 <sup>+70</sup> <sub>-70</sub>	-3.31 <sup>+0.34</sup> <sub>-0.35</sub>	2860.4(2825.2)	-0.52 <sup>+0.1</sup> <sub>-0.1</sub>	-1.74 <sup>+0.05</sup> <sub>-0.05</sub>	33 <sup>+4</sup> <sub>-4</sub>	570 <sup>+90</sup> <sub>-80</sub>	-3.33 <sup>+0.4</sup> <sub>-0.35</sub>	67 <sup>+40</sup> <sub>-35</sub>	2853.4(2806.6)	7
19	21	-0.63 <sup>+0.13</sup> <sub>-0.13</sub>	-1.75 <sup>+0.08</sup> <sub>-0.09</sub>	33 <sup>+6</sup> <sub>-6</sub>	450 <sup>+90</sup> <sub>-90</sub>	-3 <sup>+0.4</sup> <sub>-0.4</sub>	2781.7(2746.5)	-0.66 <sup>+0.1</sup> <sub>-0.1</sub>	-1.81 <sup>+0.08</sup> <sub>-0.08</sub>	35 <sup>+6</sup> <sub>-6</sub>	530 <sup>+150</sup> <sub>-140</sub>	-3.2 <sup>+0.5</sup> <sub>-0.5</sub>	60 <sup>+23</sup> <sub>-23</sub>	2774.5(2727.7)	7.2
21	23	-0.57 <sup>+0.1</sup> <sub>-0.1</sub>	-1.79 <sup>+0.05</sup> <sub>-0.05</sub>	31 <sup>+4</sup> <sub>-4</sub>	350 <sup>+50</sup> <sub>-50</sub>	-3.2 <sup>+0.31</sup> <sub>-0.32</sub>	2822.7(2787.5)	-0.59 <sup>+0.09</sup> <sub>-0.1</sub>	-1.84 <sup>+0.07</sup> <sub>-0.08</sub>	33 <sup>+4</sup> <sub>-4</sub>	350 <sup>+80</sup> <sub>-70</sub>	-3.2 <sup>+0.4</sup> <sub>-0.4</sub>	68 <sup>+23</sup> <sub>-27</sub>	2814.3(2767.5)	8.4
23	25	-0.52 <sup>+0.1</sup> <sub>-0.1</sub>	-1.75 <sup>+0.05</sup> <sub>-0.05</sub>	31 <sup>+4</sup> <sub>-4</sub>	390 <sup>+50</sup> <sub>-50</sub>	-3.25 <sup>+0.32</sup> <sub>-0.31</sub>	2836.4(2801.2)	-0.53 <sup>+0.11</sup> <sub>-0.11</sub>	-1.78 <sup>+0.06</sup> <sub>-0.06</sub>	32 <sup>+4</sup> <sub>-4</sub>	410 <sup>+80</sup> <sub>-70</sub>	-3.3 <sup>+0.4</sup> <sub>-0.4</sub>	62 <sup>+22</sup> <sub>-27</sub>	2829.1(2782.2)	7.3
25	27	-0.53 <sup>+0.12</sup> <sub>-0.12</sub>	-1.86 <sup>+0.05</sup> <sub>-0.05</sub>	28.1 <sup>+3.3</sup> <sub>-3.4</sub>	330 <sup>+70</sup> <sub>-70</sub>	-3.6 <sup>+0.5</sup> <sub>-0.5</sub>	2718.9(2683.7)	-0.54 <sup>+0.12</sup> <sub>-0.12</sub>	-1.87 <sup>+0.06</sup> <sub>-0.06</sub>	28.1 <sup>+3.4</sup> <sub>-3.4</sub>	290 <sup>+90</sup> <sub>-100</sub>	-3.5 <sup>+0.6</sup> <sub>-0.6</sub>	63 <sup>+40</sup> <sub>-32</sub>	2706.8(2660.1)	12.1
27	29	-0.56 <sup>+0.17</sup> <sub>-0.18</sub>	-1.78 <sup>+0.2</sup> <sub>-0.17</sub>	22 <sup>+4</sup> <sub>-5</sub>	108 <sup>+30</sup> <sub>-27</sub>	-3.1 <sup>+0.6</sup> <sub>-0.6</sub>	2643.6(2608.4)	-0.7 <sup>+0.5</sup> <sub>-0.6</sub>	-1.1 <sup>+0.7</sup> <sub>-0.6</sub>	14 <sup>+8</sup> <sub>-7</sub>	76 <sup>+11</sup> <sub>-15</sub>	-2.69 <sup>+0.25</sup> <sub>-0.19</sub>	69 <sup>+14</sup> <sub>-13</sub>	2628.7(2581.9)	14.9
29	31	-0.81 <sup>+0.32</sup> <sub>-0.3</sub>	-0.9 <sup>+0.4</sup> <sub>-0.4</sub>	15 <sup>+9</sup> <sub>-9</sub>	64 <sup>+5</sup> <sub>-5</sub>	-2.29 <sup>+0.06</sup> <sub>-0.06</sub>	2601.8(2566.6)	-0.88 <sup>+0.4</sup> <sub>-0.31</sub>	-0.8 <sup>+0.4</sup> <sub>-0.4</sub>	13 <sup>+7</sup> <sub>-7</sub>	62 <sup>+5</sup> <sub>-5</sub>	-2.31 <sup>+0.07</sup> <sub>-0.06</sub>	45 <sup>+17</sup> <sub>-19</sub>	2594.1(2547.2)	7.7
31	33	-0.37 <sup>+0.24</sup> <sub>-0.24</sub>	-1.81 <sup>+0.18</sup> <sub>-0.15</sub>	15.5 <sup>+2.4</sup> <sub>-2.5</sub>	75 <sup>+19</sup> <sub>-18</sub>	-2.8 <sup>+0.4</sup> <sub>-0.4</sub>	2616.2(2581)	-0.8 <sup>+0.5</sup> <sub>-0.5</sub>	-1.2 <sup>+0.7</sup> <sub>-0.7</sub>	12 <sup>+5</sup> <sub>-5</sub>	58 <sup>+9</sup> <sub>-10</sub>	-2.6 <sup>+0.23</sup> <sub>-0.22</sub>	63 <sup>+21</sup> <sub>-20</sub>	2605.6(2558.8)	10.6
33	35	-0.45 <sup>+0.27</sup> <sub>-0.23</sub>	-1.72 <sup>+0.14</sup> <sub>-0.21</sub>	21 <sup>+5</sup> <sub>-5</sub>	116 <sup>+28</sup> <sub>-27</sub>	-3 <sup>+0.5</sup> <sub>-0.5</sub>	2633.9(2598.7)	-0.51 <sup>+0.32</sup> <sub>-0.24</sub>	-1.59 <sup>+0.19</sup> <sub>-0.34</sub>	20 <sup>+5</sup> <sub>-5</sub>	105 <sup>+28</sup> <sub>-29</sub>	-2.9 <sup>+0.4</sup> <sub>-0.4</sub>	49 <sup>+21</sup> <sub>-21</sub>	2627.4(2580.5)	6.5
35	37	-0.56 <sup>+0.15</sup> <sub>-0.15</sub>	-1.89 <sup>+0.05</sup> <sub>-0.06</sub>	24.9 <sup>+3.3</sup> <sub>-3.1</sub>	230 <sup>+50</sup> <sub>-60</sub>	-3.6 <sup>+0.6</sup> <sub>-0.6</sub>	2640.5(2605.3)	-0.55 <sup>+0.13</sup> <sub>-0.14</sub>	-1.91 <sup>+0.06</sup> <sub>-0.06</sub>	24.9 <sup>+2.8</sup> <sub>-2.8</sub>	190 <sup>+70</sup> <sub>-80</sub>	-3.4 <sup>+0.6</sup> <sub>-0.6</sub>	60 <sup>+28</sup> <sub>-28</sub>	2631.5(2584.6)	9
37	39	-0.53 <sup>+0.23</sup> <sub>-0.23</sub>	-1.83 <sup>+0.08</sup> <sub>-0.09</sub>	19 <sup>+4</sup> <sub>-4</sub>	135 <sup>+24</sup> <sub>-24</sub>	-3.5 <sup>+0.5</sup> <sub>-0.5</sub>	2606.6(2571.4)	-0.55 <sup>+0.23</sup> <sub>-0.22</sub>	-1.82 <sup>+0.08</sup> <sub>-0.11</sub>	18.9 <sup>+4</sup> <sub>-3.4</sub>	119 <sup>+29</sup> <sub>-30</sub>	-3.5 <sup>+0.5</sup> <sub>-0.5</sub>	52 <sup>+22</sup> <sub>-22</sub>	2597.9(2551.1)	8.7
39	41	-0.29 <sup>+0.3</sup> <sub>-0.25</sub>	-1.8 <sup>+0.07</sup> <sub>-0.15</sub>	17.5 <sup>+0.26</sup> <sub>-0.26</sub>	99 <sup>+26</sup> <sub>-24</sub>	-3.2 <sup>+0.5</sup> <sub>-0.8</sub>	2557.7(2522.5)	-0.23 <sup>+0.3</sup> <sub>-0.28</sub>	-1.81 <sup>+0.14</sup> <sub>-0.13</sub>	17.1 <sup>+0.26</sup> <sub>-0.26</sub>	84 <sup>+24</sup> <sub>-24</sub>	-3.2 <sup>+0.5</sup> <sub>-0.5</sub>	51 <sup>+25</sup> <sub>-24</sub>	2547.1(2500.3)	10.6
41	43	-1 <sup>+0.5</sup> <sub>-0.4</sub>	-1.1 <sup>+0.6</sup> <sub>-0.4</sub>	9 <sup>+5</sup> <sub>-5</sub>	66 <sup>+7</sup> <sub>-7</sub>	-2.44 <sup>+0.08</sup> <sub>-0.15</sub>	2578.5(2543.3)	-1.1 <sup>+0.5</sup> <sub>-0.4</sub>	-1 <sup>+0.8</sup> <sub>-0.6</sub>	7 <sup>+4</sup> <sub>-4</sub>	65 <sup>+11</sup> <sub>-9</sub>	-3.4 <sup>+0.4</sup> <sub>-0.4</sub>	93 <sup>+13</sup> <sub>-11</sub>	2563.5(2516.7)	15
43	45	-0.4 <sup>+0.4</sup> <sub>-0.4</sub>	-1.2 <sup>+0.4</sup> <sub>-0.4</sub>	9 <sup>+5</sup> <sub>-4</sub>	38.9 <sup>+3</sup> <sub>-3</sub>	-2.31 <sup>+0.18</sup> <sub>-0.24</sub>	2511.5(2476.3)	-0.48 <sup>+0.35</sup> <sub>-0.4</sub>	-1.26 <sup>+0.27</sup> <sub>-0.27</sub>	13 <sup>+6</sup> <sub>-8</sub>	37 <sup>+3.2</sup> <sub>-3.1</sub>	-2.67 <sup>+0.21</sup> <sub>-0.2</sub>	58 <sup>+18</sup> <sub>-19</sub>	2504(2457.1)	7.5
45	50	-0.4 <sup>+0.5</sup> <sub>-0.8</sub>	-1.3 <sup>+0.8</sup> <sub>-0.5</sub>	12.2 <sup>+3.4</sup> <sub>-4</sub>	49 <sup>+7</sup> <sub>-6</sub>	-2.47 <sup>+0.16</sup> <sub>-0.17</sub>	3520.4(3485.1)	-0.3 <sup>+0.28</sup> <sub>-0.29</sub>	-1.54 <sup>+0.29</sup> <sub>-0.28</sub>	12.9 <sup>+3.2</sup> <sub>-4</sub>	44 <sup>+5</sup> <sub>-6</sub>	-2.53 <sup>+0.19</sup> <sub>-0.18</sub>	49 <sup>+17</sup> <sub>-18</sub>	3512.7(3465.8)	7.7
50	70	-0.2 <sup>+0.5</sup> <sub>-0.5</sub>	-1.64 <sup>+0.11</sup> <sub>-0.27</sub>	11.2 <sup>+1.5</sup> <sub>-1.8</sub>	51 <sup>+8</sup> <sub>-9</sub>	-2.66 <sup>+0.28</sup> <sub>-0.3</sub>	4977.5(4942.3)	-0.1 <sup>+0.5</sup> <sub>-0.5</sub>	-1.66 <sup>+0.21</sup> <sub>-0.19</sub>	10.9 <sup>+1.6</sup> <sub>-2.4</sub>	43 <sup>+6</sup> <sub>-7</sub>	-2.64 <sup>+0.25</sup> <sub>-0.25</sub>	42 <sup>+16</sup> <sub>-17</sub>	4968.1(4921.2)	9.4

TABLE 3  
THE CALCULATED FLUX AND DERIVED PARAMETERS OF GRB 211211A PROMPT EMISSION.

$t_1$ (s)	$t_2$ (s)	$F_{\text{BB}}$ ( $10^{-6}$ erg cm $^{-2}$ s $^{-1}$ )	$F_{\text{obs}}$ ( $10^{-6}$ erg cm $^{-2}$ s $^{-1}$ )	$F_{\text{BB}}/F_{\text{obs}}$	$\Gamma_{\text{ph}}$	$R_{\text{ph}}$ ( $10^{10}$ cm)
0.5	1.5	$0.03^{+0.07}_{-0.02}$	$0.48^{+0.06}_{-0.06}$	$0.06^{+0.15}_{-0.05}$	$86.93^{+31.69}_{-20.19}$	$0.61^{+0.66}_{-0.42}$
1.5	2.5	$0.32^{+0.62}_{-0.28}$	$13.30^{+0.30}_{-0.20}$	$0.02^{+0.05}_{-0.02}$	$176.23^{+49.35}_{-31.14}$	$2.02^{+1.69}_{-1.07}$
2.5	3.5	$8.16^{+1.54}_{-1.66}$	$54.40^{+0.50}_{-0.40}$	$0.15^{+0.03}_{-0.03}$	$268.67^{+15.01}_{-15.22}$	$2.33^{+0.39}_{-0.40}$
3.5	4.5	$0.91^{+3.69}_{-0.85}$	$39.70^{+0.30}_{-0.70}$	$0.02^{+0.09}_{-0.02}$	$252.02^{+137.33}_{-58.45}$	$2.06^{+3.36}_{-1.43}$
4.5	5.5	$0.28^{+0.65}_{-0.25}$	$13.90^{+0.30}_{-0.10}$	$0.02^{+0.05}_{-0.02}$	$192.10^{+65.90}_{-40.46}$	$1.63^{+1.67}_{-1.03}$
5.5	6.5	$2.98^{+1.82}_{-1.99}$	$63.00^{+1.00}_{-0.30}$	$0.05^{+0.03}_{-0.03}$	$273.76^{+48.23}_{-49.10}$	$2.55^{+1.35}_{-1.37}$
6.5	7.5	$0.70^{+2.20}_{-0.66}$	$81.50^{+0.50}_{-0.50}$	$0.01^{+0.03}_{-0.01}$	$311.73^{+154.09}_{-100.38}$	$2.23^{+3.31}_{-2.16}$
7.5	8.5	$4.80^{+2.00}_{-2.10}$	$62.20^{+0.50}_{-0.40}$	$0.08^{+0.03}_{-0.03}$	$267.11^{+27.37}_{-27.73}$	$2.71^{+0.83}_{-0.84}$
8.5	9.5	$0.15^{+0.88}_{-0.14}$	$15.10^{+0.30}_{-0.20}$	$0.01^{+0.06}_{-0.01}$	$221.40^{+174.20}_{-73.68}$	$1.15^{+2.72}_{-1.15}$
9.5	10.5	$0.08^{+0.35}_{-0.07}$	$12.70^{+0.20}_{-0.20}$	$0.01^{+0.03}_{-0.01}$	$204.54^{+117.81}_{-54.60}$	$1.23^{+2.13}_{-0.99}$
10.5	11.5	$0.28^{+0.96}_{-0.27}$	$9.24^{+0.19}_{-0.17}$	$0.03^{+0.10}_{-0.03}$	$192.26^{+97.56}_{-58.06}$	$1.08^{+1.64}_{-0.98}$
11.5	12.5	$0.04^{+0.12}_{-0.03}$	$3.85^{+0.11}_{-0.10}$	$0.01^{+0.03}_{-0.01}$	$148.01^{+65.21}_{-37.63}$	$0.98^{+1.32}_{-0.75}$
12.5	13.5	$0.03^{+0.07}_{-0.02}$	$2.03^{+0.08}_{-0.08}$	$0.01^{+0.03}_{-0.01}$	$125.75^{+49.89}_{-28.54}$	$0.85^{+1.01}_{-0.58}$
13.5	15	$0.02^{+0.06}_{-0.02}$	$2.20^{+0.08}_{-0.06}$	$0.01^{+0.03}_{-0.01}$	$127.76^{+52.29}_{-30.06}$	$0.87^{+1.07}_{-0.62}$
15	17	$0.03^{+0.09}_{-0.03}$	$3.90^{+0.10}_{-0.04}$	$0.01^{+0.02}_{-0.01}$	$145.94^{+61.89}_{-36.96}$	$1.04^{+1.32}_{-0.79}$
17	19	$0.10^{+0.47}_{-0.09}$	$10.90^{+0.10}_{-0.20}$	$0.01^{+0.04}_{-0.01}$	$197.65^{+133.22}_{-63.08}$	$1.17^{+2.37}_{-1.12}$
19	21	$0.14^{+0.30}_{-0.12}$	$9.57^{+0.13}_{-0.14}$	$0.01^{+0.03}_{-0.01}$	$173.16^{+57.02}_{-37.15}$	$1.53^{+1.51}_{-0.98}$
21	23	$0.25^{+0.42}_{-0.22}$	$9.22^{+0.12}_{-0.13}$	$0.03^{+0.05}_{-0.02}$	$169.90^{+46.13}_{-34.54}$	$1.56^{+1.27}_{-0.95}$
23	25	$0.13^{+0.35}_{-0.12}$	$10.70^{+0.13}_{-0.17}$	$0.01^{+0.03}_{-0.01}$	$182.36^{+69.38}_{-38.22}$	$1.46^{+1.67}_{-0.92}$
25	27	$0.07^{+0.33}_{-0.06}$	$6.40^{+0.12}_{-0.12}$	$0.01^{+0.05}_{-0.01}$	$175.75^{+121.45}_{-59.16}$	$0.98^{+2.03}_{-0.99}$
27	29	$0.38^{+0.26}_{-0.31}$	$3.36^{+0.08}_{-0.08}$	$0.11^{+0.08}_{-0.09}$	$125.82^{+16.68}_{-17.90}$	$1.40^{+0.56}_{-0.60}$
29	31	$0.02^{+0.06}_{-0.02}$	$2.81^{+0.07}_{-0.06}$	$0.01^{+0.02}_{-0.01}$	$138.25^{+51.92}_{-29.94}$	$0.88^{+0.99}_{-0.57}$
31	33	$0.17^{+0.17}_{-0.15}$	$2.43^{+0.06}_{-0.07}$	$0.07^{+0.07}_{-0.06}$	$122.80^{+25.81}_{-24.50}$	$1.09^{+0.69}_{-0.65}$
33	35	$0.04^{+0.12}_{-0.03}$	$2.28^{+0.07}_{-0.08}$	$0.02^{+0.05}_{-0.02}$	$128.03^{+56.02}_{-30.89}$	$0.90^{+1.18}_{-0.65}$
35	37	$0.08^{+0.19}_{-0.07}$	$3.36^{+0.10}_{-0.08}$	$0.02^{+0.06}_{-0.02}$	$143.44^{+55.25}_{-37.13}$	$0.94^{+1.09}_{-0.73}$
37	39	$0.06^{+0.17}_{-0.05}$	$2.46^{+0.08}_{-0.08}$	$0.02^{+0.07}_{-0.02}$	$128.31^{+54.07}_{-30.66}$	$0.97^{+1.22}_{-0.69}$
39	41	$0.05^{+0.16}_{-0.04}$	$1.95^{+0.06}_{-0.07}$	$0.02^{+0.08}_{-0.02}$	$123.11^{+60.78}_{-33.25}$	$0.87^{+1.28}_{-0.70}$
41	43	$0.48^{+0.11}_{-0.14}$	$1.74^{+0.07}_{-0.07}$	$0.28^{+0.06}_{-0.08}$	$120.34^{+9.17}_{-9.59}$	$0.83^{+0.19}_{-0.20}$
43	45	$0.08^{+0.10}_{-0.07}$	$1.05^{+0.05}_{-0.04}$	$0.08^{+0.09}_{-0.06}$	$104.86^{+22.62}_{-19.58}$	$0.76^{+0.49}_{-0.42}$
45	50	$0.04^{+0.08}_{-0.03}$	$1.16^{+0.03}_{-0.04}$	$0.03^{+0.07}_{-0.03}$	$108.06^{+32.72}_{-22.00}$	$0.76^{+0.69}_{-0.47}$
50	70	$0.02^{+0.04}_{-0.01}$	$0.52^{+0.02}_{-0.02}$	$0.03^{+0.08}_{-0.02}$	$91.12^{+33.68}_{-18.95}$	$0.57^{+0.63}_{-0.36}$



TABLE 4  
DERIVED PARAMETERS OF GRB 211211A IN HYBRID JET MODEL.

$t_1$ (s)	$t_2$ (s)	$1 + \sigma_0$	$\eta$	$R_{\text{ph}}$ ( $10^{10}$ cm)	$\Gamma_{\text{ph}}$	$1 + \sigma_{\text{ph}}$
0.5	1.5	11.57	26.46	0.51	71.17	4.31
1.5	2.5	21.71	38.16	1.54	131.05	6.34
2.5	3.5	4.18	97.49	2.59	291.33	1.40
3.5	4.5	28.45	57.89	1.41	167.94	9.83
4.5	5.5	31.82	42.32	1.09	125.05	10.79
5.5	6.5	12.63	73.34	2.17	227.15	4.09
6.5	7.5	82.86	57.57	1.15	156.42	30.56
7.5	8.5	7.31	79.44	2.68	256.82	2.27
8.5	9.5	87.35	45.45	0.56	105.38	37.76
9.5	10.5	122.25	36.58	0.56	91.13	49.18
10.5	11.5	27.43	51.29	0.71	123.36	11.43
11.5	12.5	76.10	28.70	0.51	75.17	29.12
12.5	13.5	59.24	25.84	0.47	68.10	22.53
13.5	15	73.64	24.71	0.46	65.66	27.77
15	17	89.47	26.48	0.53	71.80	33.07
17	19	91.10	38.27	0.58	94.59	36.94
19	21	42.91	34.85	0.95	105.14	14.25
21	23	22.60	39.56	1.15	121.69	7.36
23	25	54.28	35.86	0.85	103.18	18.91
25	27	80.90	35.89	0.49	85.97	33.85
27	29	4.65	40.46	1.57	137.02	1.38
29	31	94.71	25.78	0.43	66.13	37.00
31	33	8.88	36.59	1.01	110.63	2.94
33	35	42.08	28.19	0.55	75.94	15.66
35	37	32.97	34.42	0.61	89.68	12.68
37	39	29.91	30.00	0.65	83.59	10.76
39	41	30.64	29.34	0.57	79.06	11.40
41	43	2.63	54.13	1.00	141.83	...
43	45	9.28	33.40	0.67	91.03	3.41
45	50	21.26	28.19	0.55	76.05	7.90
50	70	24.26	24.05	0.39	61.14	9.56

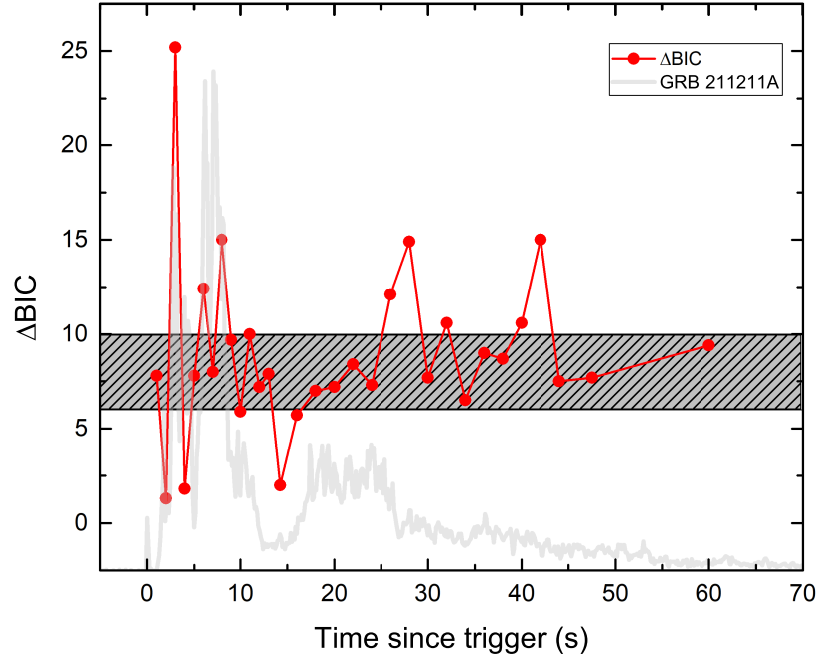


FIG. 1.—  $\Delta BIC$  (solid red circles) between 2SBPL and 2SBPL+BB models in the time-resolved spectral of GRB 211211A. The gray line is the light curve of prompt emission, and the shaded area indicates the range of [6-10].

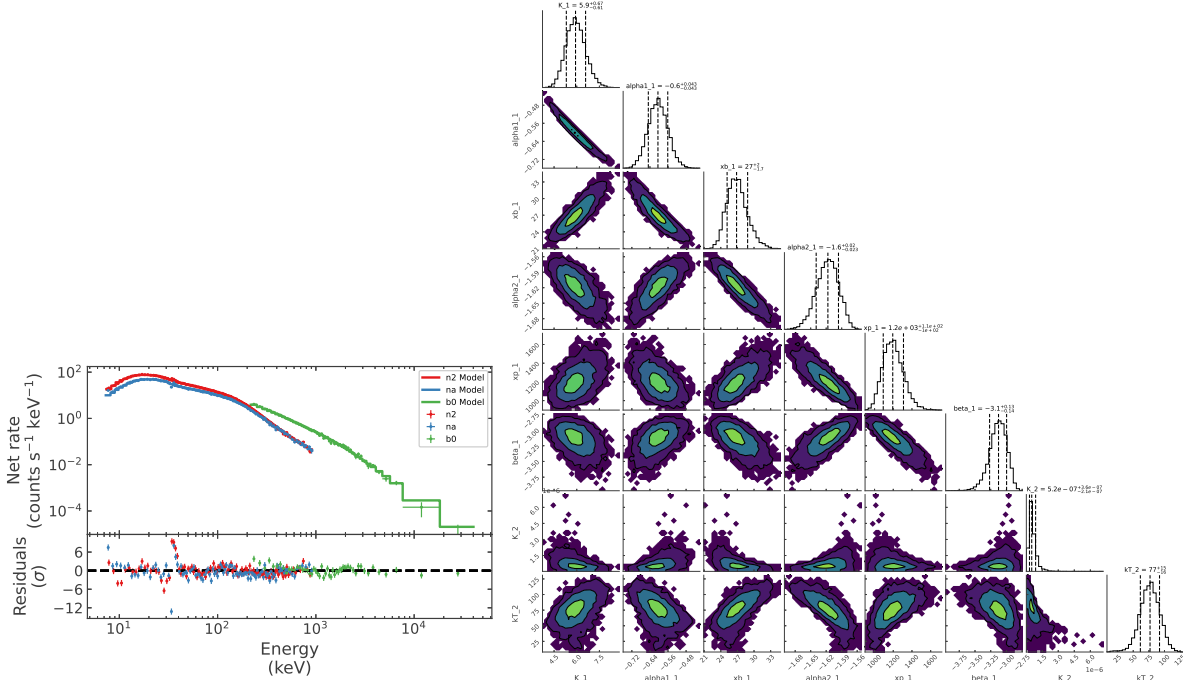


FIG. 2.— Time-integrated spectrum measured from  $T_0 + 0.5$  to  $T_0 + 70$  s is fitted by 2SBPL+BB model. Left: Observed and modeled photon count spectra. Right: the parameter constraints of the spectral fit.

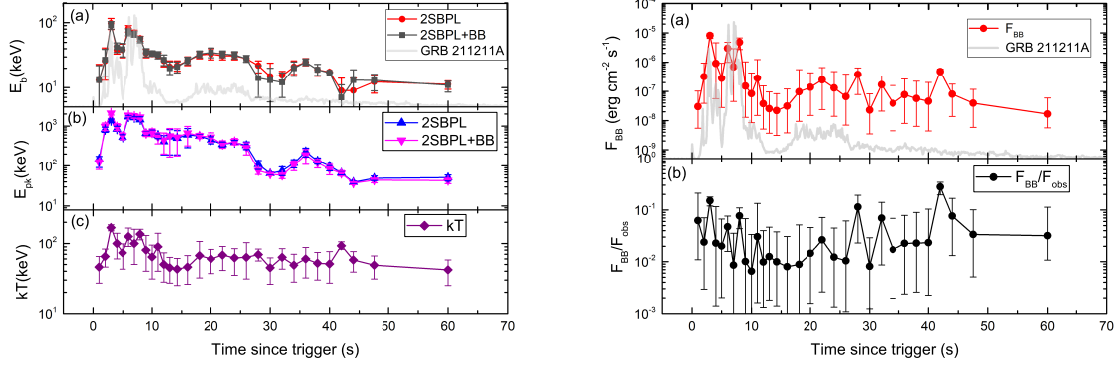


FIG. 3.— Left: Temporal evolution of  $E_b$ ,  $E_{pk}$  and  $kT$  of 2SBPL+BB model. Right: Similar to left panels, but for the flux ( $F_{BB}$ ) of BB emission and  $F_{BB}/F_{obs}$ .

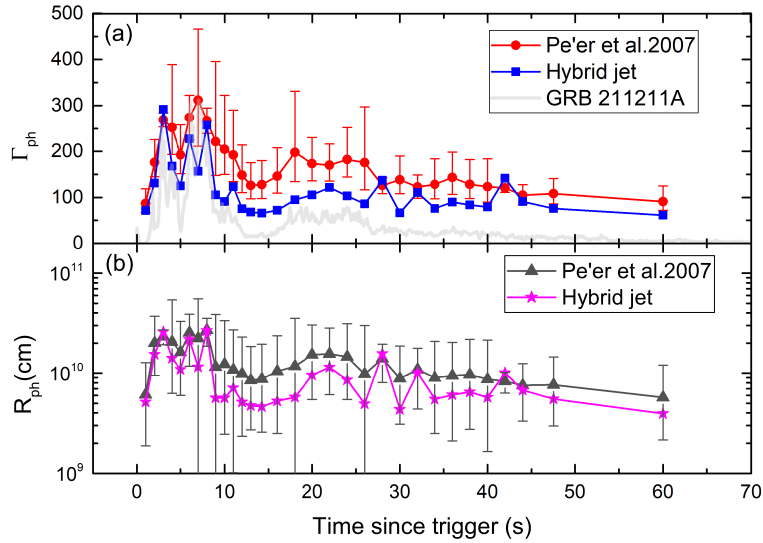


FIG. 4.— Temporal evolution of derived parameters  $\Gamma_{ph}$  and  $R_{ph}$  by using Pe'er et al. (2007) model and hybrid jet (Gao & Zhang 2015).

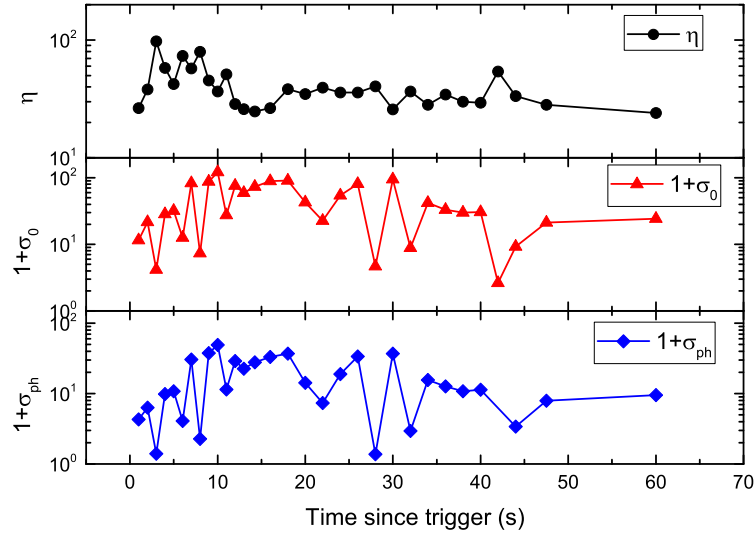


FIG. 5.— Temporal evolution of  $1 + \sigma_0$ ,  $\eta$ , and  $1 + \sigma_{\text{ph}}$  in the hybrid jet model for fixed  $r_0 = 10^7$  cm.

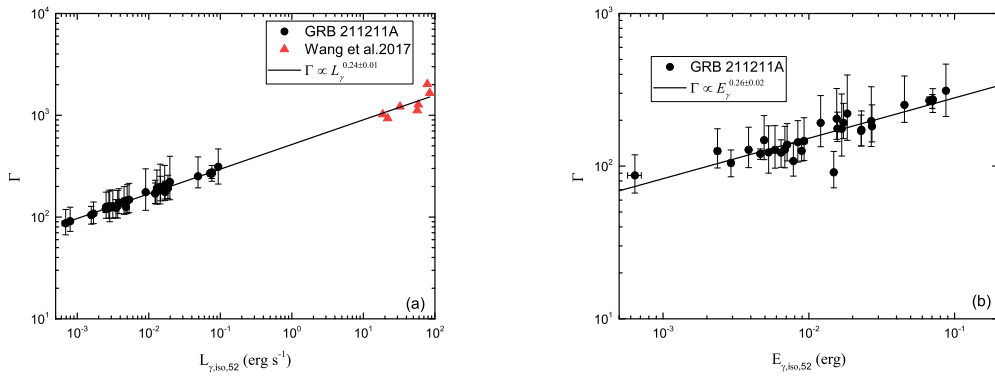


FIG. 6.— Lorentz Factor ( $\Gamma_{\text{ph}}$ ) as a function of  $L_{\gamma,\text{iso}}$  (a) and  $E_{\gamma,\text{iso}}$  of GRB 211211A (black solid circles). The black solid lines are the best fit with power-law model. The red triangles are the data of GRB 160625B from Wang et al. (2017).